A state-dependant constitutive model for methane hydrate-bearing sediments inside the stability region

Author's affiliation and address:

Name: Charles Wang Wai Ng
Affiliation: CLP Holdings Professor of Sustainability
Address: Department of Civil and Environmental Engineering, Hong Kong University of Science and Technology, Clear Water Bay, Kowloon, Hong Kong
E-mail:cecwwng@ust.hk

Name: Sina Baghbanrezvan*
Affiliation: PhD Student
Address: Department of Civil and Environmental Engineering, Hong Kong University of Science and Technology, Clear Water Bay, Kowloon, Hong Kong
E-mail:sbad@connect.ust.hk

Name: Tomas Kadlicek
Affiliation: PhD Student
Address: Faculty of Civil Engineering, Czech Technical University in Prague, Thákurova 2077/7, 160 00 Praha 6, Czech Republic
E-mail:tomas.kadlicek@fsv.cvut.cz

Name: Chao Zhou
Affiliation: Research Assistant Professor
Address: Department of Civil and Environmental Engineering, Hong Kong University of Science and Technology, Clear Water Bay, Kowloon, Hong Kong
E-mail:cezhou@ust.hk

Dr. Chao Zhou, affiliated with the Hong Kong Polytechnic University at the time of final publication.

ABSTRACT

The presence of methane hydrate in soil pores alters the stress-strain and volumetric behaviour of soil. The extent of this alteration is affected by the temperature and pore-pressure state of methane hydrate inside the thermodynamically stable region. In this paper, a state-dependent critical state model is developed for methane hydrate-bearing sediments (MHBS) within the theoretical framework of bounding surface plasticity. A phase parameter is newly introduced into the constitutive model to account for the coupled effects of temperature and pore pressure on the mechanical behaviour of MHBS. This unique feature of the proposed model enables it to capture the behaviour of MHBS inside the methane hydrate stability region. A non-associated flow rule is adopted and a modified dilatancy expression is proposed considering the degree of hydrate saturation, morphology, phase parameter and stress state of MHBS. To verify the new model, computed results are compared to measured results of drained triaxial tests on MHBS with different morphologies and at different effective confining stresses, degrees of hydrate saturation and phase states inside the stability region. The comparison reveals that the model is capable of capturing the key features such as the evident strain softening behaviour due to hydrate degradation and the change in stress-strain and volumetric behaviour of MHBS at different initial conditions inside the stability region.

KEYWORDS: Methane hydrate-bearing sediments; constitutive relations; methane hydrate stability

INTRODUCTION

Methane hydrates are the most commonly occurring gas hydrates and are typically found in permafrost and marine soil sediments in areas such as Canada, the South China Sea, the Nankai Trough in Japan, and the Korean East Sea. (Waite *et al*., 2009). Their natural abundance makes them a potential source of energy for the future. This has probed the interest of engineers and researchers to investigate the influence of methane hydrate on soil behaviour to ensure well-designed off-shore infrastructure and safe extraction methods. A distinct characteristic of methane hydrates is that they are only stable under thermodynamically favourable conditions (i.e. relatively high pore pressures and low temperatures). The stability region for methane hydrate is shown in Fig. 1(a) (Sloan and Koh, 2007).

Previous experimental studies have found that methane hydrate contributes significantly to the mechanical behaviour of the sediment bearing it (Miyazaki *et al*., 2011; Clayton *et al*., 2010; Hyodo *et al*., 2013b, Yun *et al*., 2007; Santamarina *et al*., 2015). The dependence of methane hydrate strength and stability on temperature and pore pressure might pose a challenge to the serviceability of offshore structures (Hovland & Gudmestad, 2001) or cause certain geohazards such as submarine landslides (Waite *et al*., 2009). This is an important aspect of the behaviour of methane hydrate-bearing sediments (MHBS) since experimental results have revealed that an increase in temperature from 1 to 10°C will result in a 19% decrease in peak shear strength for water-saturated MHBS (Hyodo *et al*. 2013b). The temperature dependence is even more pronounced for gas-saturated MHBS—a change in temperature from 1 to 5°C will lead to a 29% drop in peak shear strength. On the other hand, an increase in pore pressure from 5 to 10 MPa will cause the peak shear strength of water- and gas-saturated MHBS to rise by 6 and 40% respectively (Hyodo *et al*. 2013a; 2013b). Hence, it is crucial to simulate the complex behaviour of MHBS at different phase states inside the stability region. Over the past decade,

several constitutive models have been proposed for MHBS, some of which are discussed below.

Klar *et al*. (2010) developed a model within the Mohr-Coulomb failure framework by considering the effects of hydrate saturation (i.e. the ratio of the volume of hydrate to the volume of voids) on the cohesion term. However, the Mohr-Coulomb models are unable to capture some of the key features of soil behaviour such as strain softening, volumetric yielding and plastic strains prior to failure. Uchida *et al*. (2012) showed that the limitations of the Mohr-Coulomb models for MHBS can cause volume changes during the dissociation stage to be underestimated. The behaviour of Mohr-Coulomb models was later improved to account for the strain softening behaviour of MHBS by considering the degradation of the cohesion term with plastic deformation (Pinkert and Grozic, 2014; Pikert *et al*., 2015).

A number of elastoplastic models have been developed within the critical state framework. Sultan and Garziglia (2011) incorporated the effects of hydrate saturation into the modified cam clay (MCC) model by expanding the yield surface solely due to increases in preconsolidation pressure. However, the cohesion produced by hydrate bonding and the softening behaviour due to hydrate degradation were not considered. The progressive hydrate degradation and the true cohesion imparted by the hydrate bonds are considered in the extended MCC model by Uchida *et al*. (2012). The model performance was validated using hydrates with two different morphologies in soil. However, an associated flow rule was assumed and the effects of internal state were not considered in the dilatancy function. This might pose challenges in simulating the mechanical behaviour of methane hydrates in sand sediments at different states and the associated flow rule is deemed unsuitable for the modelling of sand behaviour (Collins, 2002). The extended MCC model proposed by Yan and Wei (2017) incorporates a non-associated flow rule. One of the main features of this model is that it

considers the dependence of MHBS behaviour on the hydrate morphology. However, the model is not able to capture satisfactorily the dilative volumetric behaviour of sand without hydrate on the dry side of the critical state line. Shen *et al*. (2016) proposed a state-dependent critical state model which is able to capture the behaviour of MHBS at different levels of hydrate saturation, void ratio and effective confining stress with a single set of parameters. However, the volumetric yielding cannot be captured given the yield surface employed in the model. Sanchez *et al*. (2017) developed a hierarchical single surface elastoplastic model for MHBS. They incorporated inelastic mechanisms which improved the modelling of MHBS during dissociation. Lin *et al*. (2015) developed a spatially-mobilized-plane subloading critical state model for MHBS. This model is able to capture the mechanical behaviour of MHBS with different levels of hydrate saturation and different hydrate morphologies. As far as the authors are aware, a constitutive model has yet to emerge that considers the dependence of hydrate strength on the hydrate state inside the stability region.

In this study a new state-dependent critical state model for MHBS is developed. This is the first constitutive model incorporating the dependence of MHBS on the phase state inside the stability region. The model is based on the theoretical framework of bounding surface plasticity (Dafalias, 1986), which accounts for the plastic deformation inside the bounding surface. A modified state-dependent dilatancy is introduced to account for the hydrate saturation, stress level, internal state and phase state inside the stability region. The model formulation and calibration are presented in detail. Recently published experimental data on MHBS with different morphologies and at different effective confining stresses, degrees of hydrate saturation, temperatures, and pore pressures are adopted to evaluate the model performance.

MATHEMATICAL FORMULATIONS

Basic relationships

The model is formulated in the triaxial stress space and defined in terms of six constitutive variables: mean effective stress (p'), deviator stress (q), degree of hydrate saturation (S_h), specific volume (υ), temperature (T) and pore pressure (pp) as follows:

$$p' = \frac{\sigma'_1 + 2\sigma'_3}{3} \tag{1}$$

$$q = \sigma'_1 - \sigma'_3 \tag{2}$$

$$S_h = \frac{V_h}{V_v} \tag{3}$$

$$\upsilon = 1 + e \tag{4}$$

$$e = \frac{V_h + V_v}{V_s} \tag{5}$$

where σ'_1 is major principal stress, σ'_3 is minor principal stress, V_h is the volume of hydrate, V_h is the volume of voids, V_s is the volume of soil particles and e is the void ratio. Experimental data reported in the literature (Hyodo *et al*., 2013a, 2013b; Song *et al*., 2010) revealed that the strength, dilatancy and stiffness of MHBS at constant effective stress and a constant degree of hydrate saturation will increase with pore pressure. On the other hand, as temperature rises, these mechanical properties will decrease. Jiang *et al*. (2014) introduced a distance parameter in a dimensionless temperature-pressure space. In their discrete element

method (DEM) simulations, the bond strength and stiffness of hydrate were related to the distance parameter through some empirical equations. In other words, one may relate the mechanical properties of hydrate in soil pores to the minimum distance of the current state of hydrate (in terms of pore pressure and temperature) from the phase change curve.

As far as the authors are aware, none of the existing constitutive models considers changes in the mechanical properties of hydrate inside the stability region. In this study, the dependence of these mechanical properties on temperature and pore pressure is modelled with a phase parameter that is defined in the same way as the distance parameter (Jiang *et al*. 2014). This model aims to capture the behaviour of marine sediments at temperatures above 273 K. It is assumed that the pore space of soil contains hydrate-water (i.e. water-saturated MHBS) or hydrate-gas (i.e. gas-saturated MHBS) while permafrost MHBS with pore space containing gas, ice and hydrate are not considered. Dimensionless temperature and pore pressure values are obtained by normalising their actual values with respect to 245 K and 1 MPa, respectively. These normalisation values are adopted to more closely fit the phase change curve with a simple polynomial function of order 3 (Fig. 1b). The phase parameter $\left(L\right)$ can be derived by minimizing the following function:

$$L = \min\left(\sqrt{\left(\frac{T_1 - T}{245}\right)^2 + \left(\frac{pp_1 - pp}{1}\right)^2}\right) \tag{6}$$

where T_1 (K) and pp_1 (MPa) are the temperature and pore pressure of the current state of MHBS, respectively; and pp is the pore pressure on the phase boundary and can be expressed as a third-order polynomial function of T (Fig. 1b). The coordinates of the point on the phase boundary curve with a minimum distance to the current temperature-pressure state can be

obtained by either differentiating the right-hand side of equation (6) with respect to T or using the Newton iterative method.

Elastoplasticity

The model is developed within the theoretical framework of bounding surface plasticity (Dafalias 1986). Unlike most elastoplastic models, the models within this framework allow for the progressive development of plasticity inside the yield surface. Consequently, development of both elastic and plastic strains inside the yield surface leads to a smooth transition between elastic and elastoplastic behaviour. The total incremental strains can be decomposed into elastic and plastic strains as follows:

$$d\varepsilon_v = d\varepsilon_v^e + d\varepsilon_v^p \tag{7}$$

$$d\varepsilon_q = d\varepsilon_q^e + d\varepsilon_q^p \tag{8}$$

where $d\varepsilon_v$ and $d\varepsilon_q$ are the total incremental volumetric and shear strains, respectively; and the superscripts ‘e’ and ‘p’ denote the elastic and plastic components of strain, respectively. The thermal component of strain due to the expansion and contraction of soil particles, fluid and hydrate is not considered in the current model. This simplification may not affect the results of the current study significantly since the temperature range of the studied MHBS is limited (i.e. 274 K to 284 K). However, this strain component should be considered if the soil is subjected to high temperature changes after dissociation. The elastic components of strain increments for MHBS can be expressed as follows:

$$d\varepsilon_v^e = \frac{dp}{K_{sh}} \tag{9}$$

$$d\varepsilon_q^e = \frac{dq}{3G_{0h}} \tag{10}$$

where K_{sh} is the bulk modulus and G_{0h} is the shear modulus at very small strains for MHBS.

The effects of void ratio and stress state on a very small strain shear modulus (G_{0s}) and on the elastic bulk modulus (K_s) for soil without hydrate are expressed by the following relationships:

$$G_{0s} = G_{ref}\left(1+e\right)^{-3}\left(\frac{p'}{p_r}\right)^{0.5} \tag{11}$$

$$K_s = G\frac{2\left(1+\nu\right)}{3\left(1-2\nu\right)} \tag{12}$$

where G_{0s} is very small strain shear modulus of soil without hydrate; G_{ref} is the soil parameter representing the shear modulus at the reference pressure; p_r is the reference pressure (1 kPa), and ν is Poisson's ratio. The selection of equation (11) is based on extensive experimental results in previous studies on both fine-grained and coarse-grained soils without hydrate (Oztoprak & Bolton, 2013; Vardanega & Bolton, 2013).

The presence of hydrate in soil pores enhances the shear modulus and its effects on cementing hydrate morphology are more pronounced than those of the pore-filling morphology (Clayton *et al*., 2005; Clayton *et al*., 2010; Dai *et al*., 2012). The contribution of gas hydrate to shear modulus can be expressed as follows:

$$G_{0h} = G_{ref}\left(1+e\right)^{-3}\left(\frac{p'}{p_r}\right)^{0.5}\left(\frac{p_{0h}}{p'}\right)^{\vartheta^*(\chi+\xi)} \tag{13}$$

where G_{0h} is the very small strain shear modulus of MHBS; p_{0h} is the preconsolidation pressure of MHBS and the ratio of ($\frac{p_{0h}}{p'}$) represents the effects of the apparent overconsolidation ratio on G_{0h}; and ϑ is a dimensionless soil parameter. The two indices of χ and ξ will be presented later. The elastic bulk modulus of MHBS (K_{sh}) can be obtained by replacing equation (13) into the shear modulus of soil without hydrate in equation (12). Note that the model assumes that Poisson's ratio (ν) is independent of the degree of hydrate saturation.

The incremental plastic strains are expressed as follows:

$$d\varepsilon_v^p = D_s \Lambda_s \tag{14}$$

$$d\varepsilon_q^p = \Lambda_s \tag{15}$$

where $D_s = d\varepsilon_v^p \Big/ \left| d\varepsilon_q^p \right|$ is the dilatancy index; and Λ_s is the nonnegative loading index. The dilatancy and loading indices can be obtained from the flow rule and the hardening law, respectively. These indices will be determined later.

Critical state line

Triaxial test results on MHBS suggest that the critical state line (CSL) in the $\upsilon - lnp'$ plane shifts toward a higher void ratio (parallel to the CSL of soil without hydrate) as the degree of hydrate saturation increases (Hyodo *et al*. 2013b). Based on these observations, the CSL is modelled by the following expression:

$$\Gamma = \Gamma^* - \lambda \ln\left(\frac{p'}{p_r}\right) + \chi \tag{16}$$

where Γ and Γ^* are intercepts of the CSL in the $\upsilon - lnp'$ plane at the reference pressure for MHBS and soil without hydrate, respectively; λ is the gradient of the CSL in the $\upsilon - lnp'$ plane which is assumed parallel to the normal compression line and independent of hydrate saturation; and χ represents the effect of hydrate saturation, temperature and pore pressure (i.e. the phase parameters) on the shift of the CSL. The extent of this shift is affected by the hydrate morphology as well as the current temperature and pore pressure (Hyodo *et al*., 2013a, 2013b). The CSL of MHBS shifts towards a lower void ratio with an increase in temperature, a decrease in pore pressure and a decrease in the degree of hydrate saturation. The schematic of the typical experimental results for soil without hydrate and MHBS is qualitatively illustrated in Fig. 2. Thus, the following expression is proposed for the shift of the CSL:

$$\chi = b_h \left(1+L\right)^c \left[\exp\left(bS_h\right) - 1\right] \tag{17}$$

where b_h, c, and b are material parameters; and S_h is the actual degree of hydrate saturation defined in equation (3). The change in the extent of the shift of the CSL can be obtained by differentiating equation (17) as follows:

$$d\chi = h\left(L\right) b_h b \exp\left(bS_h\right) dS_h + b_h c \left(1+L\right)^{c-1} \left[\exp\left(bS_h\right) - 1\right] dL \tag{18}$$

where $h\left(L\right)$ is a Heaviside function of phase parameter (L) with $h\left(L\right) = 0$ for $L > 0$ and $h\left(L\right) = 1$ for $L = 0$. This function shows that while the temperature and pressure of MHBS are within the stability region, the change in χ is affected by a change in the phase parameter and

the initial degree of hydrate saturation (S_h). As the hydrate phase state reaches the phase boundary curve (dissociation induced by an increase in temperature or a decrease in pore pressure), the change in χ becomes a function of a change in the degree of hydrate saturation.

The CSL of the soil with hydrate in the $p'-q$ plane is expressed as follows:

$$q = Mp' \tag{19}$$

where M is the gradient of the CSL in the $p'-q$ plane. Experimental data on MHBS suggest that the value of M might be affected by the presence of hydrate in the pore space of the soil. The increase in M is less than 8% as the degree of hydrate saturation increases from 0 to 53% (Hyodo *et al*. 2013a). Shen *et al*. (2016) proposed an expression considering the dependence of M on the degree of hydrate saturation. However, their analysed data of M show large scattering and the effects of hydrate morphology, temperature and pore pressure on M remain unknown. For simplicity, it is assumed that M is independent of the hydrate saturation in the current model. Similar simplification is made in a number of constitutive models in the literature (Uchida *et al*., 2012; Lin *et al*., 2015; Yan & Wei, 2017; Sanchez *et al*., 2017).

Normal compression line

The compressibility of saturated bonded soils such as cemented and structured soils decreases significantly with increasing bonding (Burland, 1990; Cuccovillo & Coop, 1999). On the other hand, the development of plastic volumetric and shear strains results in the degradation of bonding and hence alters the mechanical properties such as strength, stiffness and compressibility (Cuccovillo & Coop, 1997). There is a lack of data on the normal compression line (NCL) of MHBS but it may be described in a similar way to bonded soils owing to their similarities. Pore occupation by gas hydrates and particle bonding can contribute to a decrease

in compressibility. As illustrated in Fig. 2, it is assumed that the NCL of soil shifts to the same extent as the CSL when gas hydrates occupy pores. In addition, particle bonding shifts the NCL of MHBS (with hydrate inside the pores) towards a higher void ratio. Hence, the NCL of MHBS can be described by the following expression:

$$N = N^* - \lambda \ln\left(\frac{p'}{p_r}\right) + \chi + \xi \tag{20}$$

where N and N^* are intercepts of the NCL at the reference pressure in the $\upsilon - lnp'$ plane for MHBS and soil, respectively; and ξ represents the shift of the NCL due to particle bonding. The initial shift of the NCL due to bonding (ξ_0) can be defined as:

$$\xi_0 = a^* \chi_0 \tag{21}$$

where a is a material parameter and χ_0 is the initial shift of the CSL. The last term in equation (20), which is attributed to particle bonding (ξ), can be degraded due to plastic deformation as well as the change in the phase parameter and the degree of hydrate saturation. The evolution of bonding is modelled as follows:

$$d\xi = \xi\left(-x\sqrt{d\varepsilon_s^{p2} + d\varepsilon_v^{p2}} + d\chi / \chi\right) \tag{22}$$

where x is the degradation factor. The plastic shear and volumetric strains are considered to contribute equally to the degradation of the bonding structure. This assumption might be approximately true and equation (22) can be modified by the addition of a weighting factor to strain increments which require further experimental data.

Bounding surface

By adopting the bounding surface plasticity theory of Dafalias (1986), a similar expression to that for the bounding surface, which has been widely used for soil without gas hydrate under isothermal (Yu *et al.*, 2007; Kan *et al.*, 2014) and non-isothermal (Zhou & Ng, 2015) conditions, can be defined for the bounding surface of MHBS as follows:

$$F = \left(\frac{q}{M(p' + p_b)} \right)^n + \frac{\ln\left[(p' + p_b) / (p_{0h} + p_b) \right]}{\ln r} \tag{23}$$

where n is the model parameter controlling the shape of the bounding surface; r is the spacing ratio controlling the point of intersection of the CSL and the bounding surface in the $p' - q$ plane; p_{0h} is the yield stress of MHBS, and p_b is the bonding stress defined as follows:

$$p_b = p_{b0} \ \xi \tag{24}$$

where p_{b0} is a material parameter. Parameter r can be deduced from the vertical spacing of the CSL and NCL as follows:

$$r = \exp\left[\frac{(N^* - \Gamma^*) + \xi}{\lambda - \kappa} \right] \tag{25}$$

This parameter is constant and set to 2.718 and 2.0 in the original Cam-clay model and modified Cam-clay model, respectively. The variations in the shape of the bounding surface with respect to the change in parameters r and n are illustrated in Zhou & Ng (2015). The typical shape of the bounding surface for MHBS and soil without gas hydrate is shown in Fig. 3. The size and location of the bounding surface for MHBS are controlled by the two parameters representing

the yield stress (p_{0h}) and the bonding stress (p_b), respectively. An increase in the degree of hydrate saturation and the phase parameter will cause the bounding surface to expand. This is reflected in equations (20) and (21) by increasing p_{0h} and ξ_0. Degradation of hydrates is modelled through the decrease in ξ, which causes the bounding surface to contract. The effects of different hydrate morphologies on the bounding surface are reflected by the parameters ξ and S_{he} (different CSLs and NCLs) as well as a change in the initial bonding stress ($p_{b0}\xi_0$).

Mapping rule

For any given stress state inside the bounding surface, dilatancy, plastic moduli and the loading index are all dependent on the image stress state (Dafalias, 1986). The image stress state is in essence the projection of the actual stress state onto the bounding surface (Fig. 4). A proper mapping rule is required for the models developed within the theoretical framework of bounding surface plasticity. It specifies the plastic moduli at the actual stress state in terms of both the plastic moduli on the bounding surface and the distance between the actual and image stress states (Dafalias, 1986). The radial mapping rule is employed in the current model due to its simplicity and versatility for a wide range of stress paths (Dafalias 1986). As illustrated in Fig. 4, the mapping origin MO ($-p_b$, 0) is defined as the left intersection point of the bounding surface with the p'-axis. A similar mapping origin is defined for cemented soils by Yang *et al.* (2008) using a translated coordinate system. The image stress state B ($\overline{p}'$, $\overline{q}$) is determined by the projection of the actual stress state $\mathrm{A}(p', q)$ onto the bounding surface with respect to the mapping origin. The two Euclidean distances of the actual and image stress states from the mapping origin can be expressed as follows:

$$\rho = \sqrt{q^2 + (p' + p_b)^2} \tag{26}$$

$$\bar{\rho} = \sqrt{\bar{q}^2 + (\bar{p}' + p_b)^2} \tag{27}$$

where ρ and $\bar{\rho}$ are the Euclidean distances of the actual and image stress states, respectively. The ratio of the two distances will later be employed to define the plastic moduli, dilatancy and the loading index inside the bounding surface.

Flow rule

A non-associated flow rule is assumed and the following general form of the state-dependent dilatancy expression (Li & Dafalias, 2000) is adopted:

$$D_s = D_s\left(\eta, e, Q, C\right) \tag{28}$$

where η is the stress ratio; Q denotes internal state variables and C denotes a set of intrinsic material constants. Following equation (28), Li & Dafalias (2000) expressed the dilatancy for a clean sand as follows:

$$D_s = \frac{d_0}{M}\left(M \exp\left(m\psi\right) - \eta\right) \tag{29}$$

where d_0 and m are two material parameters; η is the stress ratio defined as $\eta = q / p'$; and ψ is the state parameter representing the vertical distance of the soil state from the CSL in the $\upsilon - lnp'$ plane (Fig. 5) with $\psi > 0$ (State B) and $\psi < 0$ (State A) for contractive and dilative tendencies, respectively. In the current model, the following dilatancy expression is proposed for MHBS to incorporate the effects of gas hydrate, phase parameter and mapping rule:

$$D_s = \frac{d_1}{M_m}\left[M\left(\frac{\rho}{\bar{\rho}}\right)^{\beta_{DS}} \exp(n_d\psi) - M_m \right] \tag{30}$$

where d_1 , n_d and β_{DS} are material parameters; and M_m is the stress ratio defined as $M_m = q/(p' + p_b)$. The term $(\rho/\bar{\rho})$ belongs to the group Q in the general dilatancy expression (equation 28) representing the internal state variables other than the void ratio (Li, 2002) and it equals 1 when the stress state reaches the bounding surface.

Hardening law and consistency condition

The evolution of the size of the bounding surface is dependent on the change in plastic volumetric strain as well as the change in phase parameter and degree of hydrate saturation. By using Fig. 2, the hardening law can be expressed as follows:

$$dp_{0h} = p_{0h}\left(\frac{\upsilon}{\lambda-\kappa} d\varepsilon_v^p + \frac{1}{\lambda-\kappa} d\xi + \frac{1}{\lambda-\kappa} d\chi \right) \tag{31}$$

Note that $d\xi$ and $d\chi$ in equation (31) can be substituted by equations (18) and (22).

The consistency condition is derived as follows:

$$\frac{\partial F}{\partial p'} dp' + \frac{\partial F}{\partial q} dq + \frac{\partial F}{\partial p_{0h}} \frac{\partial p_{0h}}{\partial \chi} d\chi + \frac{\partial F}{\partial p_{0h}} \frac{\partial p_{0h}}{\partial \xi} d\xi + \frac{\partial F}{\partial p_{0h}} \frac{\partial p_{0h}}{\partial \varepsilon_v^p} d\varepsilon_v^p + \frac{\partial F}{\partial p_b} \frac{\partial p_b}{\partial \xi} d\xi + \frac{\partial F}{\partial r} \frac{\partial r}{\partial \xi} d\xi = 0 \tag{32}$$

Substituting equations (14), (15) and (22) into equation (32) yields:

$$\frac{\partial F}{\partial p'}dp'+\frac{\partial F}{\partial q}dq+\frac{\partial F}{\partial p_{0h}}\frac{\partial p_{0h}}{\partial \chi}d\chi+\frac{\partial F}{\partial p_{0h}}\frac{\partial p_{0h}}{\partial \xi}\xi\left(-x\Lambda_s\sqrt{1+D_s^{\,2}}+d\chi/\chi\right)$$
$$+\frac{\partial F}{\partial p_{0h}}\frac{\partial p_{0h}}{\partial \varepsilon_v^p}D_s\Lambda_s+\frac{\partial F}{\partial p_b}\frac{\partial p_b}{\partial \xi}\xi\left(-x\Lambda_s\sqrt{1+D_s^{\,2}}+d\chi/\chi\right) \quad (33)$$
$$+\frac{\partial F}{\partial r}\frac{\partial r}{\partial \xi}\xi\left(-x\Lambda_s\sqrt{1+D_s^{\,2}}+d\chi/\chi\right)=0$$

According to Dafalias (1986) the plastic modulus can be derived from the consistency condition as follows:

$$K_p=-\left(\frac{\partial F}{\partial p_{0h}}\frac{\partial p_{0h}}{\partial \varepsilon_v^p}D_s-\xi x\sqrt{1+D_s^{\,2}}\left(\frac{\partial F}{\partial p_{0h}}\frac{\partial p_{0h}}{\partial \xi}+\frac{\partial F}{\partial p_b}\frac{\partial p_b}{\partial \xi}+\frac{\partial F}{\partial r}\frac{\partial r}{\partial \xi}\right)\right) \quad (34)$$

Likewise, the loading index can be obtained as follows:

$$\Lambda_s=\frac{1}{K_p}\left(\frac{\partial F}{\partial p'}dp'+\frac{\partial F}{\partial q}dq+\frac{\partial F}{\partial p_{0h}}\frac{\partial p_{0h}}{\partial \chi}d\chi+d\chi/\chi\left(\frac{\partial F}{\partial p_{0h}}\frac{\partial p_{0h}}{\partial \xi}+\frac{\partial F}{\partial p_b}\frac{\partial p_b}{\partial \xi}+\frac{\partial F}{\partial r}\frac{\partial r}{\partial \xi}\right)\right) \quad (35)$$

Detailed derivations of the terms in equations (34) and (35) are presented in the Appendix.

The plastic modulus is obtained from equation (34) when the stress state of MHBS is on the bounding surface. The mapping rule is incorporated into the plastic modulus expression to take into account the reduction in the plastic modulus when the MHBS stress state is inside the bounding surface. Hence, equation (34) takes the following form:

$$K_p = -\frac{\partial F}{\partial p_{0h}}\frac{\partial p_{0h}}{\partial \varepsilon_v^p}\frac{d_1}{M_m}\left[M\left(\frac{\bar{\rho}}{\rho}\right)^{\beta kp}\exp\left(n_d\psi\right)-M_m\right] + \xi x\sqrt{1+\left[\frac{d_1}{M_m}\left(M\left(\frac{\bar{\rho}}{\rho}\right)^{\beta kp}\exp\left(n_d\psi\right)-M_m\right)\right]^2}\left(\frac{\partial F}{\partial p_{0h}}\frac{\partial p_{0h}}{\partial \xi}+\frac{\partial F}{\partial p_b}\frac{\partial p_b}{\partial \xi}+\frac{\partial F}{\partial r}\frac{\partial r}{\partial \xi}\right) \quad (36)$$

where β_{kp} is a material parameter. When the stress state reaches the bounding surface, the ratio of $\left(\frac{\bar{\rho}}{\rho}\right)$ approaches unity and equation (34) is recovered.

CALIBRATION OF PARAMETERS

The constitutive equations are integrated by the Euler forward (explicit) method with a sub-stepping scheme. In order to achieve a high accuracy, the size of each sub-step is determined by the procedure proposed by Sloan (1987). The phase parameter (L), which defines the minimal distance from the phase boundary curve, is determined using the Newton iterative method.

In summary, the model consists of 18 parameters. Eleven of them are for soil without hydrate which enables the model to account for state-dependant dilatancy. Eight of the parameters $(\lambda, \kappa, M, N^*, \Gamma^*, n_d, d_1, G_{ref})$ can be calibrated following the procedure proposed by Li & Dafalias (2000). The other three soil parameters ($\beta_{Ds,}\beta_{kp,}n$) are determined through back-analysis of drained triaxial test on Toyoura sand. In addition, there are seven parameters $\left(a,b,b_h,c,p_{b0},x,\vartheta\right)$ for MHBS considering the temperature-pressure dependence of hydrate, degradation of hydrate with deformation, hydrate morphology and dissociation. All of these parameters can be obtained from experimental data. The parameters b,b_h and c in equation (17) are calibrated from the following CSLs of MHBS: CSLs at different degrees of hydrate

saturation under the same temperature-pressure conditions (i.e. phase parameter) and at two different temperatures (or pore pressure) but with the same degree of hydrate saturation. The parameters a and x can be obtained from a NCL of MHBS at a known degree of hydrate saturation. The initial bonding stress ($p_{b0}\xi_0$) in equation (24) can be calculated from the results of an unconfined compression test on MHBS following the procedure by Yan & Li (2011). The parameter ϑ can be obtained by fitting equation (13) to the results of resonant column or bender element tests on shear modulus at different degrees of hydrate saturation. The parameters a, p_{b0}, x and ϑ were obtained from back-analysis of three triaxial tests, two drained triaxial tests on MHBS (with different degrees of hydrate saturation) and one drained triaxial test with different phase parameters (either at different temperature or pore pressure change), and a single set of parameters is used to capture the MHBS at various states. The soil parameters without hydrate and MHBS for different morphologies are summarised in Table. 1.

The two studies by Hyodo *et al*. (2013a; 2013b) provide complete experimental data on MHBS and are selected for the calibration and validation of the proposed model. Hyodo *et al*. (2013b) performed a series of drained triaxial compression tests on pure Toyoura sand and water-saturated MHBS. Partially water-saturated specimens of Toyoura sand were pressurized with methane gas (i.e. the excess gas method) and kept within the stability region of methane hydrate to initiate hydrate formation. The excess gas method is well known to result in forming a cementing morphology of hydrate in the sand (Waite *et al*. 2009). The subsequent saturation with water dissociates the hydrate at the grain contacts resulting in a change in the morphology of pore-filling hydrate with a weaker bonding (Hyodo *et al*., 2013). The MHBS specimens were prepared at different degrees of hydrate saturation (ranging from 0 to 60%) and isotropically consolidated to effective confining pressures of 1, 3 and 5 MPa and an average

void ratio of 0.65. The drained triaxial compression tests were conducted at different temperatures (1, 5 and 10°C) and pore pressures (5 and 10 MPa).

The second set of drained triaxial tests on gas-saturated MHBS are retrieved from Hyodo *et al*. (2013a). Methane hydrate was formed in Toyoura sand by the excess gas method while the subsequent water saturation causing hydrate dissociation at the grain contacts was not performed. The dominant methane hydrate morphology in this method was inferred to be cementing and confirmed by Yoneda *et al*. (2016) using X-ray computed tomography. The volume change of the gas-saturated specimens was measured using a double-cell system since the volume change could not be measured from the amount of water drained in the experiments. Tests were conducted on specimens with an average void ratio of 0.66. The test conditions such as the effective confining pressure, degree of hydrate saturation, temperature and pore pressure are presented in each figure.

COMPARISON BETWEEN MEASURED AND COMPUTED RESULTS

Effects of hydrate saturation on MHBS behaviour

Fig. 6 compares the measured and computed drained triaxial test results of water-saturated MHBS with different degrees of hydrate saturation. The effective confining pressure, temperature and pore pressure were kept constant in these experiments and their values are presented in the figure. As illustrated in the figure, soil with initially contractive tendency might dilate due to methane hydrate formation since the CSL of MHBS shifts towards a higher void ratio. This results in a change in the state parameter and hence the dilatancy through equation (30). The stiffness enhancement due to the presence of hydrate is reflected in equation (13) through the apparent overconsolidation ratio and the shift of the NCL. The agreement between the measured and computed results demonstrates the effectiveness of the proposed model

formulation at capturing the enhancement of shear strength, stiffness and dilatancy with increasing hydrate saturation. The calibrated parameters for MHBS are summarised in Table 1 and a single set of parameters is used for all computed results on water-saturated MHBS with pore-filling morphology.

Fig. 7 compares the measured and computed drained triaxial test results on gas-saturated specimens with different degrees of hydrate saturation. As stated earlier, the MHBS specimens with cementing and pore-filling morphologies have different stress-strain and volumetric behaviours even at the same degree of hydrate saturation. Hence, the two specimens with different morphologies may be treated as different materials with different sets of methane hydrate parameters. A similar approach is adopted in all existing constitutive models for MHBS with the ability to capture the hydrate morphology. The same set of parameters as in the previous section is used for the host sand (Toyoura sand) and a new set of parameters for the cementing morphology is calibrated and summarised in Table 1. The computed results agree satisfactorily with the measured results in terms of stress-strain and volumetric behaviours at different degrees of hydrate saturation (Fig. 7). The experimental evidence suggests that stiffness enhancement is more significant for the cementing morphology than for the pore filling morphology (Clayton *et al*. 2010). This behaviour is captured by the proposed model by introducing an apparent overconsolidation ratio in equation (13). The strain softening behaviour of the cementing morphology is more pronounced than that of the pore-filling morphology since the degradation of bonding due to plastic strains contributes to a decrease in the shear strength. Hence, a higher initial bonding stress ($p_{b0}\xi_0$) in equation (24) and a higher mechanical degradation factor (x) in equation (22) are adopted for the modelling of the cementing morphology. This enables better capturing the more significant strain softening behaviour of MHBS with cementing hydrate.

Effects of effective confining pressure on MHBS behaviour

The measured and computed results on water-saturated MHBS at different effective confining pressures are presented and compared in Fig. 8. The experiments were conducted on specimens with an average degree of hydrate saturation of 53% and a void ratio of 0.65. The temperature and pore pressure of the specimens were kept constant at 5°C and 10 MPa, respectively. The model captures the clear strain softening behaviour at an effective confining pressure of 1 MPa using the proposed state-dependent dilatancy (equation (30)) and the degradation in equation (22). The shift of the CSL to a higher void ratio due to the presence of hydrate increases the state parameter in equation (30) resulting in a dilatancy enhancement. On the other hand, the increase in dilatancy results in higher plastic volumetric strains and hence a greater degradation of hydrate through equation (20). These two aspects enable the proposed model to capture the MHBS behaviour at different stress states. Despite some discrepancy between the measured and computed peak shear strengths at effective confining pressures of 3 and 5 MPa, the overall stress-strain and volumetric behaviours of MHBS are captured satisfactorily.

Effects of phase parameter (temperature and pore pressure) on water-saturated MHBS behaviour

Figures 9 compares the measured and computed results on water-saturated MHBS at different temperatures. The specimens were tested at the same effective confining pressure of 3 MPa and an average void ratio of 0.65. The degree of hydrate saturation for each test is presented in the corresponding figure. The experimental data on the stress-strain and volumetric behaviours of MHBS reveal an evident dependence of hydrate structure on temperature and pore pressure. This behaviour cannot be captured by existing models in the literature. The effects of temperature and pore pressure on the mechanical behaviour of MHBS are reflected by a single

dimensionless phase parameter (L). As stated earlier, parameter "c" can be calibrated with two triaxial test data by either changing the temperature or the pore pressure. In the current study, the parameter "c" is calibrated for the tests at temperatures of 5 and 10°C with a constant pore pressure of 10 MPa. The other three tests at different temperatures and pore pressures are predicted with the same set of parameters. An increase in temperature (a decrease in the phase parameter (L)) results in a shift of the CSL to a lower void ratio (equation (17)). Consequently, the dilatancy of MHBS decreases due to a decrease in the state parameter (ψ). The effects of temperature on stiffness are reflected in equation (13) through an apparent overconsolidation ratio. The proposed model captures the increasing trend in stiffness and peak shear strength due to a decrease in temperature (Fig. 9). However, the dilatancy of the specimen at the temperature of 1°C is overestimated. Despite the different stress-strain behaviours, the measured volumetric strains of the specimens at the temperatures of 1 and 5°C are nearly identical. In the proposed model, it is assumed that the decrease in temperature contributes to the peak shear strength and dilatancy of MHBS. This assumption is based on analysis conducted by Jiang *et al*. (2015) on extensive experimental data on pure methane hydrate specimens at different temperatures and pore pressures. Thus, the observed discrepancy between the measured and computed results is unavoidable. The observed trend in the volumetric behaviour due to changes in temperature is further shown in the results on gas-saturated MHBS with cementing morphology. As illustrated in Fig. 10, the model predictions agree well with the measured results at different pore pressures. It should be pointed out that the two constitutive variables (i.e. the degree of hydrate saturation and pore pressure) are different in these experiments but the model is able to capture the behaviour with a single set of parameters. This is a unique feature of the proposed model compared to current existing models (Uchida *et al*., 2012; Lin *et al*., 2015; Yan & Wei, 2017; Sanchez *et al*., 2017).

Effects of phase parameter (temperature and pore pressure) on gas-saturated MHBS behaviour

As illustrated in Fig. 11, the increasing trend in dilatancy, stiffness, and peak shear strength with a decrease in temperature for gas-saturated MHBS can be captured by the proposed formulation. Due to the limited experiments on gas-saturated MHBS at different temperature-pore pressures, the parameter 'c' is calibrated through the drained triaxial tests conducted at different temperatures and the test results at different pore pressures are predicted by the model. The observed dilatancy enhancement due to the decrease in temperature supports the earlier stated assumption on the trend of the volumetric behaviour. A comparison of the results for the water-saturated (pore filling morphology) and gas-saturated (cementing morphology) specimens reveals that the gas-saturated MHBS are more dependent on temperature (Figs. 9 and 11). The more significant increase in the peak shear strength, stiffness and dilatancy of gas-saturated specimens with an increase in the phase parameter (L) is captured by equation (17) representing the extent of the shift of the CSL.

Figure 12 compares the measured and computed results at the temperature of 5°C and different pore pressures of 5 and 10 MPa. The same set of parameters are used and the new phase parameter (L) is calculated from the minimum distance from the current temperature-pore pressure state to the phase transformation boundary. The model can well capture the strain softening due to the enhanced dilation and the bonding degradation. Similar to the triaxial results at different temperatures, the higher dependence of the gas-saturated MHBS than the water-saturated MHBS is well captured by the proposed model (Figs. 9 and 11). The results of Figs. 9, 10, 12, and 13 suggest that the selection of phase parameter (L) is an effective approach to predicting the coupled effects of temperature and pore pressure on the mechanical behaviour of MHBS.

SUMMARY AND CONCLUSIONS

A new state-dependent critical state model is developed within the theoretical framework of bounding surface plasticity. This model can account for the hydrate saturation, stress level, temperature and pore pressure. A phase parameter is introduced to include the coupled effects of temperature and pore pressure on the mechanical behaviour of MHBS. This unique feature enables the model to capture the behaviour of MHBS when the temperature-pore pressure is inside the stability region and it is useful for the prediction of seabed settlement and the serviceability of pipelines and platform foundations on shallow MHBS.

The capability and accuracy of the model are demonstrated by comparing the computed results with measured drained triaxial experiments on MHBS. Two different morphologies, cementing and pore filling, were considered at different levels of effective confining pressure, hydrate saturation, and pore pressure under different temperatures. The comparison between the measured and computed results reveal that the newly proposed model is able to predict the shear strength, stiffness and dilatancy at different temperatures and pore pressures inside the stability region. The more pronounced softening behaviour in cementing hydrate than in pore-filling hydrate is well captured by the newly proposed degradation of hydrate bonding due to plastic strains. Moreover, the model is able to capture the enhanced peak shear strength, stiffness and dilatancy due to a decrease in temperature and an increase in pore pressure inside the stability region.

ACKNOWLEDGEMENTS

The authors would like to acknowledge the National Natural Science Foundation of China for research grant no. 51778166 and the Research Grants Council (RGC) of the Hong Kong Special Administrative Region (HKSAR) for research grant no. 16204817.The second author is

grateful for the support of the Hong Kong Ph.D. Fellowship Scheme (HKPFS) provided by the RGC of the HKSAR. Mr. André Archer is acknowledged for his valuable comments and discussions.

APPENDIX

The partial derivatives of the bounding surface with respect to constitutive variables in equation (34) can be obtained as:

$$\frac{\partial F}{\partial p'} = -n\left(\frac{q}{M}\right)^{n}\left(p'+p_b\right)^{-n-1} + \frac{1}{\left(p'+p_b\right)\ln r} \tag{36}$$

$$\frac{\partial F}{\partial q} = n\left(\frac{1}{M\left(p+p_b\right)}\right)^{n} q^{n-1} \tag{37}$$

$$\frac{\partial F}{\partial p_{0h}} = -\frac{1}{\ln r}\frac{1}{\left(p_{0h}+p_b\right)} \tag{38}$$

$$\frac{\partial F}{\partial p_b} = -n\left(\frac{q}{M\left(p'+p_b\right)}\right)^{n-1}\frac{q}{M\left(p'+p_b\right)^{2}} + \frac{1}{\ln r}\frac{p_{0h}-p'}{\left(p'+p_b\right)\left(p_{0h}+p_b\right)} \tag{39}$$

$$\frac{\partial p_{0h}}{\partial \xi} = p_{0h}\frac{1}{\lambda-\kappa} \tag{40}$$

$$\frac{\partial p_{0h}}{\partial \chi} = p_{0h}\frac{1}{\lambda-\kappa} \tag{41}$$

$$\frac{\partial p_{0h}}{\partial \varepsilon_v^{p}} = p_{0h}\frac{1+e}{\lambda-\kappa} \tag{42}$$

$$\frac{\partial p_b}{\partial \xi} = p_{b0} \tag{43}$$

$$\frac{\partial F}{\partial r} = -\ln\left(\frac{(p+p_b)}{(p_0+p_b)}\right) \times \frac{1}{r\left(\ln(r)\right)^2} \tag{44}$$

$$\frac{\partial r}{\partial \xi} = \frac{r}{\lambda - \kappa} \tag{45}$$

NOTATION

a, b, b_h, c	material parameters in equations (17) and (21)
C	a set of intrinsic material constants
d_0	material parameter in equation (29)
d_1	material parameters in equation (30)
D_s	dilatancy
$d\varepsilon_q$, $d\varepsilon_q^e$, $d\varepsilon_q^p$	total, elastic and plastic incremental shear strains
$d\varepsilon_v$, $d\varepsilon_v^e$, $d\varepsilon_v^p$	total, elastic and plastic incremental volumetric strains
e	void ratio
G_{0s}, G_{0h}	very small strain shear modulus of soil and MHBS
G_{ref}	shear modulus at reference pressure
$h(L)$	Heaviside function of phase parameter (L)
K_s, K_{sh}	bulk modulus of soil and MHBS
L	phase parameter
M	gradient of the CSL in the $p'-q$ plane
m	material parameter in equation (29)
M_m	stress ratio defined as $M_m = q/(p' + p_b)$
n	parameter controlling the shape of the bounding surface
N, N^*	intercepts of NCL at the reference pressure in plane for MHBS and soil
n_d	material parameter in equation (30)
p'	mean effective stress

p_{0h}	yield stress of MHBS
p_b	bonding stress
p_{b0}	material parameter in equation (24)
pp	pore pressure
p_r	reference pressure (1 kPa)
Q	internal state variables
q	deviator stress
r	spacing ratio controlling the intersection position of the critical state line and the bounding surface in the $p'-q$ plane
S_h	degree of hydrate saturation
T	temperature
$T_1(K)$, $pp_1(MPa)$	temperature and pore pressure of the current state of MHBS
v	Poisson's ratio
V_h, V_v, V_s	volume of hydrate, void and soil particles, respectively
x	degradation factor
β_{DS}, β_{Kp}	material parameters in equations (30) and (36)
Γ, Γ^*	intercepts of CSL in $\upsilon-lnp'$ plane at reference pressure for MHBS and soil without hydrate, respectively
ζ	shift of NCL due to bonding
ζ_0	initial shift of the NCL due to bonding
η	stress ratio defined as $\eta = q/p'$
ϑ	material parameter in equation (13)
λ	gradient of CSL in $\upsilon-lnp'$ plane
Λ_s	loading index
ρ, $\overline{\rho}$	Euclidean distances of the actual and image stress states, respectively
σ'_1, σ'_3	Major and minor principal stresses, respectively
υ	specific volume
χ	shift of CSL due to the effects of hydrate saturation and phase parameter
χ_0	initial shift of CSL
ψ	state parameter representing the vertical distance of the soil state from CSL in $\upsilon-lnp'$ plane

REFERENCES

Burland, J. B. (1990). On the compressibility and shear strength of natural clays. *Géotechnique*, **40**, No. 3, 329-378.

Clayton, C. R. I., Priest, J. A. & Best, A. I. (2005). The effects of disseminated methane hydrate on the dynamic stiffness and damping of a sand. *Géotechnique*, **55**, No. 6, 423–434.

Clayton, C. R. I., Priest, J. A., & Rees, E. V. L. (2010). The effects of hydrate cement on the stiffness of some sands. *Géotechnique*, ***60***, No. 6, 435–455.

Collins, I. F. (2002). Associated and non-associated aspects of the constitutive laws for coupled elastic/plastic materials. *International Journal of Geomechanics, ASCE* **2**, No. 2, 259-267.

Cuccovillo, T. & Coop, M. R. (1997). Yielding and pre-failure deformation of structured sands. *Géotechnique*, **47**, No. 3, 491–508.

Cuccovillo, T., & Coop, M. R. (1999). On the mechanics of structured sands. *Géotechnique*, **49**, No. 6, 741-760.

Dafalias, Y. F. (1986). Bounding surface plasticity. I: Mathematical foundation and hypoplasticity. *Journal of Engineering Mechanics, ASCE* **112**, 9, 966-987.

Dai, S., J. C. Santamarina, W. F. Waite, & T. J. Kneafsey (2012), Hydrate morphology: Physical properties of sands with patchy hydrate saturation, *Journal of Geophysical Research: Solid Earth 117*. **117**, B11205.

Ghiassian, H., & Grozic, J. L. (2013). Strength behavior of methane hydrate bearing sand in undrained triaxial testing. *Marine and petroleum geology*, **43**, 310-319.

Hovland, M. & Gudmestad, O.T. (2001). Potential Influence of Gas Hydrates on Seabed Installations. *Natural Gas Hydrates: Occurrence, Distribution and Detection. Geophysical Monograph* 124. *American Geophysical Union.*

Hyodo, M., Li, Y., Yoneda, J., Nakata, Y., Yoshimoto, N., Nishimura, A., & Song, Y. (2013a). Mechanical behavior of gas- saturated methane hydrate- bearing sediments. *Journal of Geophysical Research: Solid Earth*, **118**, No. 10, 5185-5194.

Hyodo, M., Yoneda, J., Yoshimoto, N., & Nakata, Y. (2013b). Mechanical and dissociation properties of methane hydrate-bearing sand in deep seabed. *Soils and foundations*, **53**, No. 2, 299-314.

Jiang, M., He, J., Wang, J., Chareyre, B., & Zhu, F. (2015). DEM Analysis of Geomechanical Properties of Cemented Methane Hydrate–Bearing Soils at Different Temperatures and Pressures. *International Journal of Geomechanics, ASCE* **16**, No. 3, 04015087.

Kan, M. E., Taiebat, H. A., & Khalili, N. (2013). Simplified mapping rule for bounding surface simulation of complex loading paths in granular materials. *International Journal of Geomechanics*, **14**, No. 2, 239-253.

Klar, A., Soga, K., & Ng, M. Y. A. (2010). Coupled deformation–flow analysis for methane hydrate extraction. *Géotechnique*, **60**, No. 10, 765-776.

Li, X. S. (2002). A sand model with state-dapendent dilatancy. *Géotechnique*, **52**, No. 3, 173-186.

Li, X. S., & Dafalias, Y. F. (2000). Dilatancy for cohesionless soils. *Géotechnique*, **50**, No. 4, 449-460.

Lin, J. S., Seol, Y., & Choi, J. H. (2015). An SMP critical state model for methane hydrate-bearing sands. *International Journal for Numerical and Analytical Methods in Geomechanics*, **39**, No. 9, 969-987.

Masui, A., Haneda, H., Ogata, Y. & Aoki, K. (2005). The effect of saturation degree of methane hydrate on the shear strength of synthetic methane hydrate sediments. *Proceedings of the 5th International Conference on Gas Hydrates, Trondheim, Norway* **2**, 657–663, paper no. 2037.

Miyazaki, K., A. Masui, Y. Sakamoto, K. Aoki, N. Tenma, and T. Yamaguchi (2011), Triaxial compressive properties of artificial methane-hydrate-bearing sediment, *Journal of geophysical research: solid earth.*, **116**, B06102.

Oztoprak, S., & Bolton, M. D. (2013). Stiffness of sands through a laboratory test database. *Géotechnique*, **63**, No. 1, 54.

Pinkert, S., & Grozic, J. L. H. (2014). Prediction of the mechanical response of hydrate-bearing sands. *Journal of Geophysical Research: Solid Earth*, **119**, No. 6, 4695-4707.

Pinkert, S., Grozic, J. L. H., & Priest, J. A. (2015). Strain-softening model for hydrate-bearing sands. *International Journal of Geomechanics, ASCE* **15**, No. 6, 04015007.

Sánchez, M., Gai, X., & Santamarina, J. C. (2017). A constitutive mechanical model for gas hydrate bearing sediments incorporating inelastic mechanisms. *Computers and Geotechnics*, **84**, 28-46.

Santamarina, J.C., Dai, S., Terzariol, M., Jang, J., Waite, W.F., Winters, W.J., Nagao, J., Yoneda, J., Konno, Y., Fujii, T. and Suzuki, K. (2015). Hydro-bio-geomechanical properties of hydrate-bearing sediments from Nankai Trough. *Marine and Petroleum Geology*, **66**, 434-450.

Shen, J., Chiu, C. F., Ng, C. W. W., Lei, G. H., & Xu, J. (2016). A state-dependent critical state model for methane hydrate-bearing sand. *Computers and geotechnics*, **75**, 1-11.

Sloan, S. W. (1987). Substepping schemes for the numerical integration of elastoplastic stress–strain relations. *International journal for numerical methods in engineering*, **24**. No. 5, 893-911.

Sloan, E. D., and C. A. Koh (2007). *Clathrate Hydrates of Natural Gases*. 3rd ed. CRC Press, Taylor and Francis Group, New York.

Song, Y., Yu, F., Li, Y., Liu, W., & Zhao, J. (2010). Mechanical property of artificial methane hydrate under triaxial compression. *Journal of Natural Gas Chemistry*, **19**, No. 3, 246-250.

Spangenberg, E., Priegnitz, M., Heeschen, K., & Schicks, J. M. (2014). Are laboratory-formed hydrate-bearing systems analogous to those in nature?. *Journal of Chemical & Engineering Data*, **60**, No. 2, 258-268.

Sultan, N. & Garziglia, S. (2011). "Geomechanical constitutive modelling of gas-hydrate-bearing sediments." In *Proceedings of the 7th International Conference on Gas Hydrates*, [online], pp. 11. Edinburgh, Scotland, U.K. July 17-21. Available at: https://www.egis.hw.ac.uk/icgh7/ [Accessed 13 June. 2018].

Uchida, S., Soga, K., & Yamamoto, K. (2012). "Critical state soil constitutive model for methane hydrate soil." *Journal of Geophysical Research: Solid Earth*, 117, No. B3, B03209.

Vardanega, P. J., & Bolton, M. D. (2013). Stiffness of clays and silts: Normalizing shear modulus and shear strain. *Journal of Geotechnical and Geoenvironmental Engineering, ASCE* **139**, No. 9, 1575-1589.

Waite, W.F., Santamarina, J.C., Cortes, D.D., Dugan, B., Espinoza, D.N., Germaine, J., Jang, J., Jung, J.W., Kneafsey, T.J., Shin, H. & Soga, K.(2009). Physical properties of hydrate- bearing sediments. *Reviews of geophysics*, **47**, No. 4, 1-38.

Yan, R., & Wei, C. (2017). Constitutive model for gas hydrate–bearing soils considering hydrate occurrence habits. *International Journal of Geomechanics, ASCE* **17**, No. 8, 04017032.

Yang, C., Cui, Y. J., Pereira, J. M., & Huang, M. S. (2008). A constitutive model for unsaturated cemented soils under cyclic loading. *Computers and Geotechnics*, **35**, No. 6, 853-859.

Yoneda, J., Jin, Y., Katagiri, J., & Tenma, N. (2016). Strengthening mechanism of cemented hydrate- bearing sand at microscales. *Geophysical Research Letters*, **43**, No. 14, 7442-7450.

Yu, H. S., Khong, C., & Wang, J. (2007). A unified plasticity model for cyclic behaviour of clay and sand. *Mechanics research communications*, **34**, No. 2, 97-114.

Yun, T. S., Santamarina, J. C. & Ruppel, C. (2007). Mechanical properties of sand, silt and clay containing tetrahydrofuran hydrate. *Journal of Geophysical Research: Solid Earth.* **112**, No. B04106, **doi**: 10.1029/2006JB004484.

Zhou, C., & Ng, C. W. W. (2015). A thermomechanical model for saturated soil at small and large strains. *Canadian Geotechnical Journal*, **52**, No. 8, 1101-1110.

Table 1. Summary of model parameters

Sand		Methane Hydrate		
Parameter	Value	Parameter	Value (Pore-filling)	Value (Cementing)
λ	0.127	a	1.5	0.7
ν	0.05	b	3.05	3.61
M	1.3	b_h	0.025	0.016
N^*	2.982	c	10	45
Γ^*	2.702	p_{b0}	2500	40000
n_d	1.6	x	6	12
d_1	1.4	ϑ	0.3	0.3
n	2	---	---	---
β_{Ds}	0.01	---	---	---
β_{kp}	1.5	---	---	---
G_{ref}	22000	---	---	---

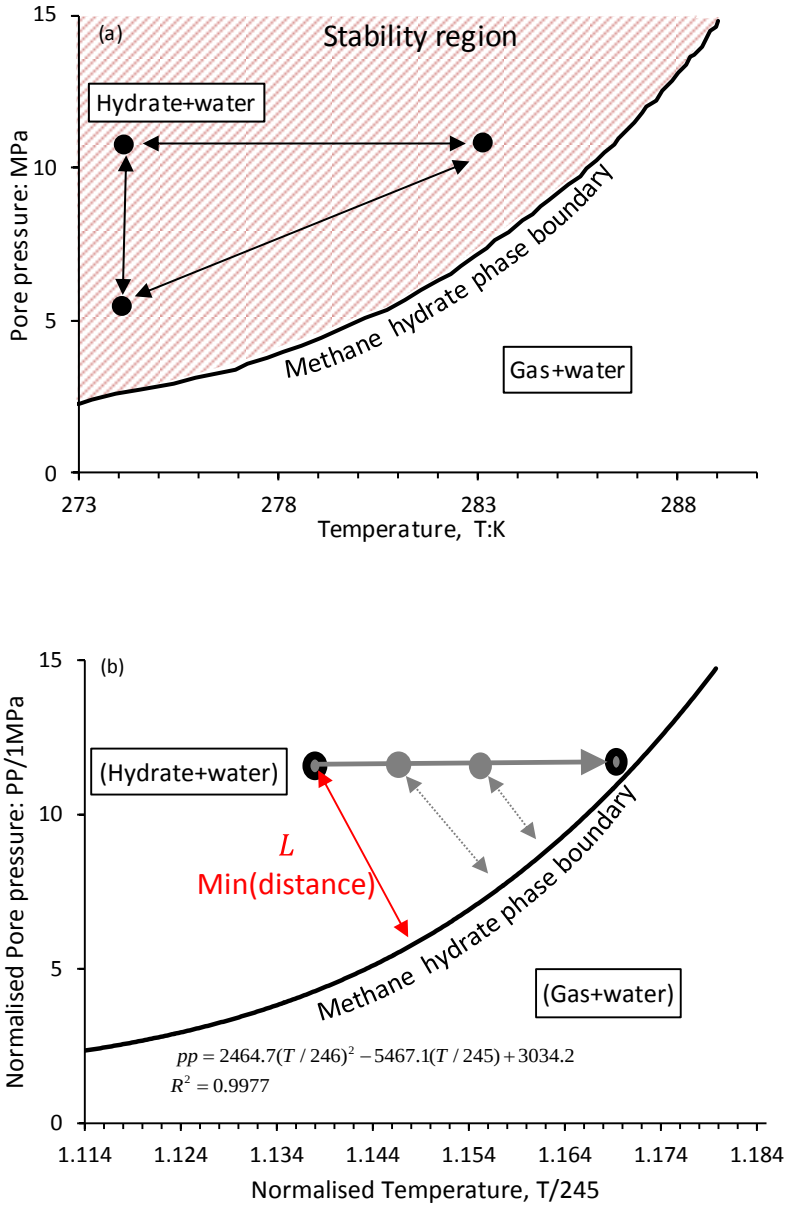

Fig. 1. Phase transformation boundary of methane hydrate: (a) actual temperature and pore pressure plane (Sloan and Koh, 2007); (b) normalised temperature and pore pressure plane

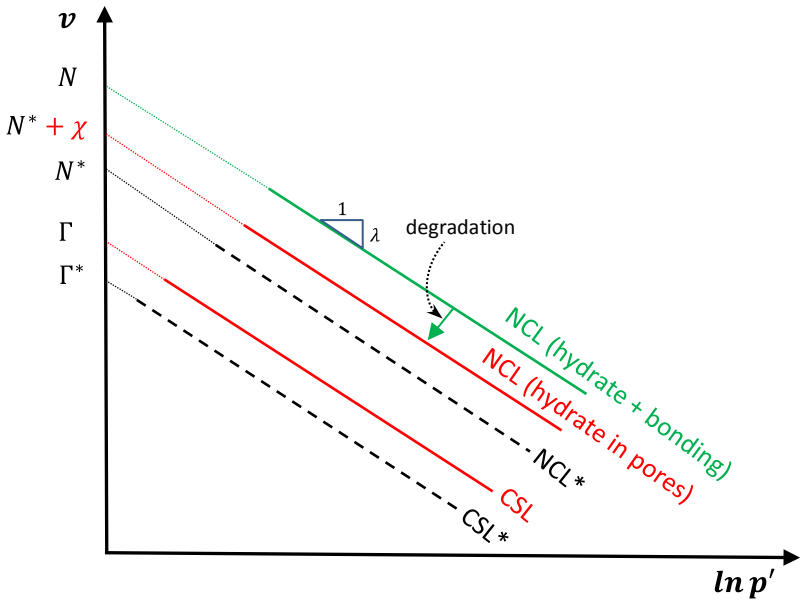

Fig. 2. Normal compression lines and critical state lines of MHBS and soil without hydrate

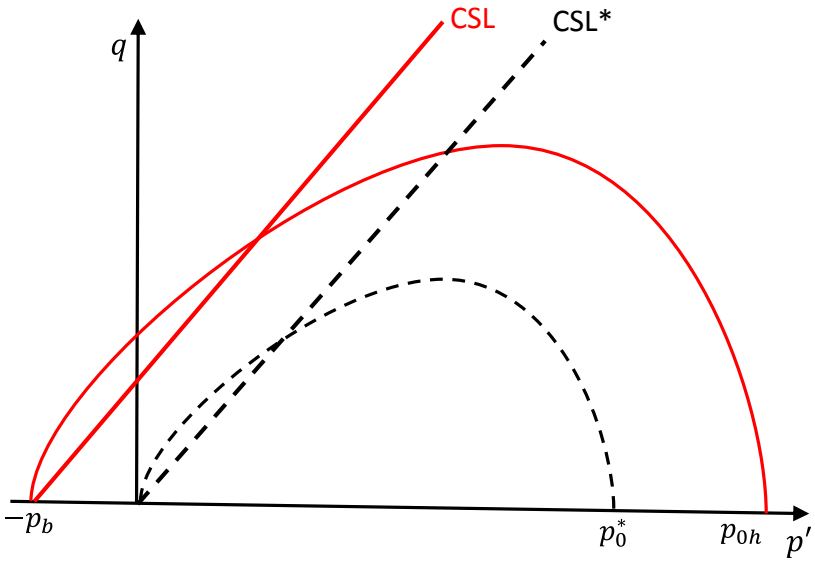

Fig. 3. Typical bounding surface of MHBS and soil without hydrate

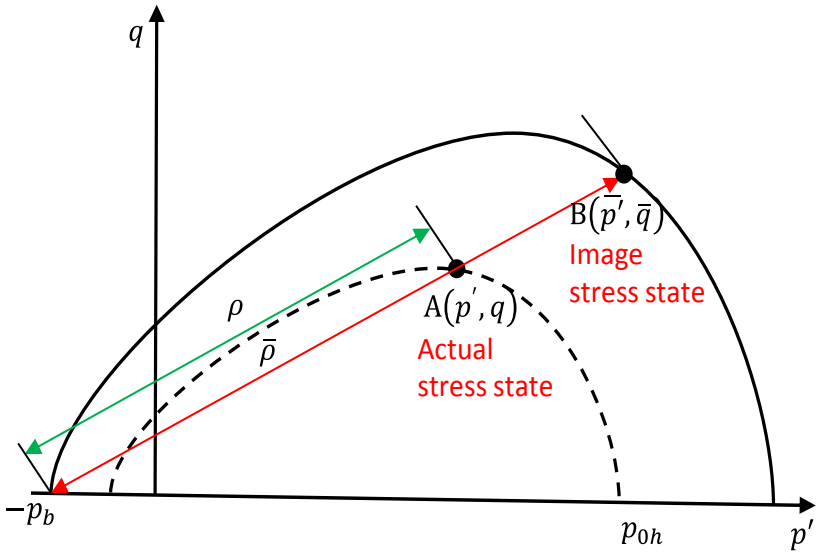

Fig. 4. Mapping rule for the bounding surface plasticity

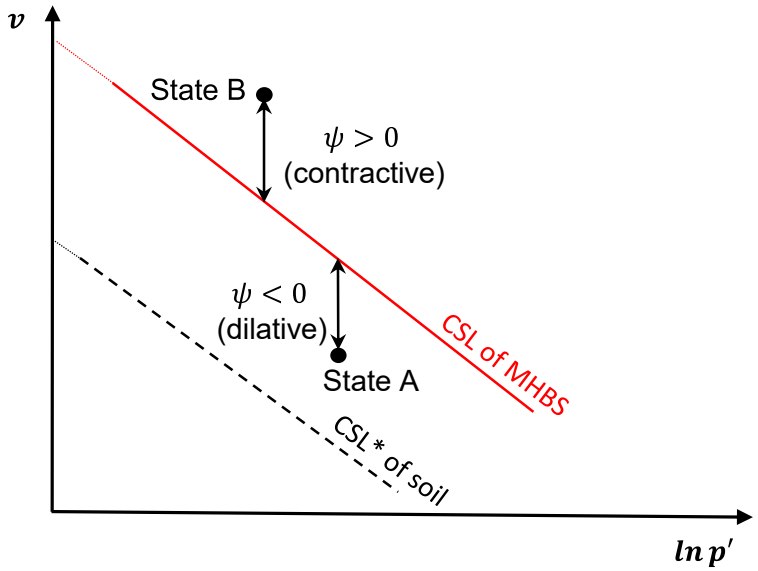

Fig. 5. Critical state line and state parameter of MHBS and soil without hydrate

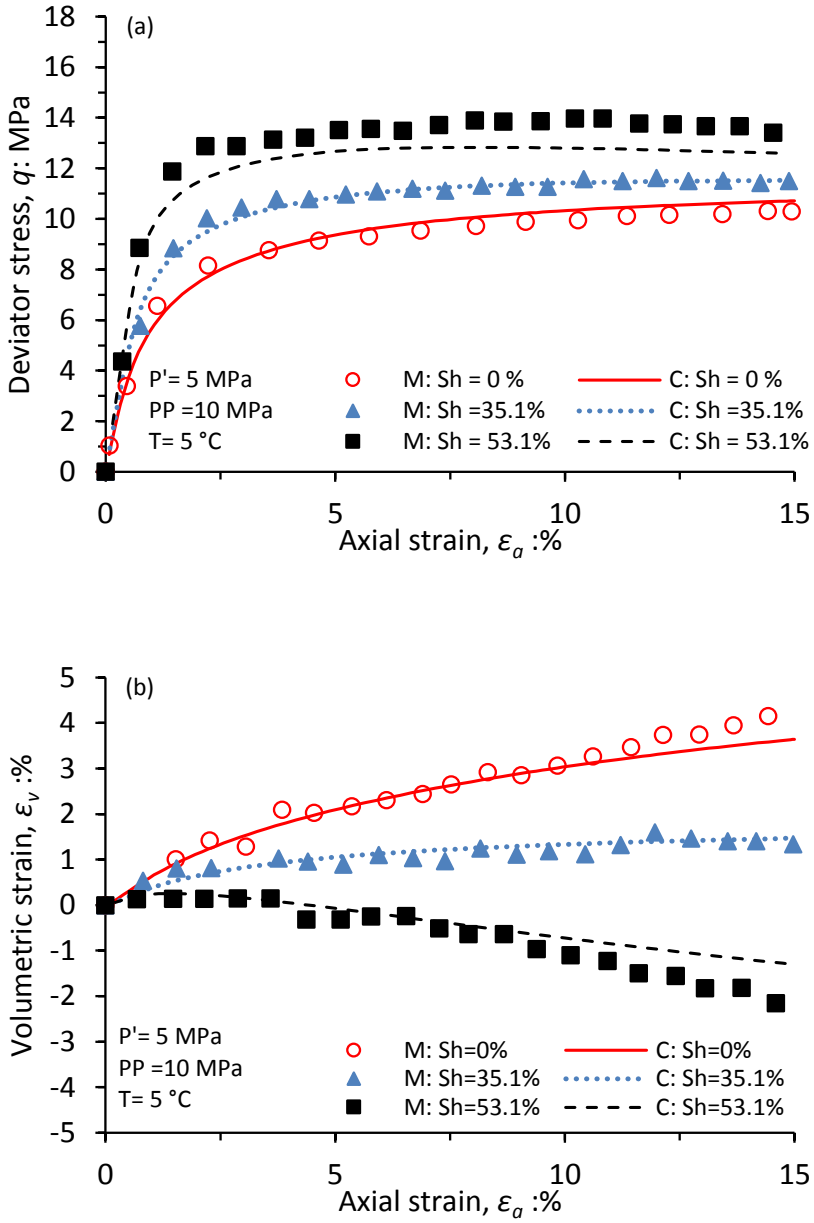

Fig. 6. Comparison of the measured and computed results of water-saturated MHBS with different degrees of hydrate saturation: (a) stress-strain behaviour; (b) volumetric response

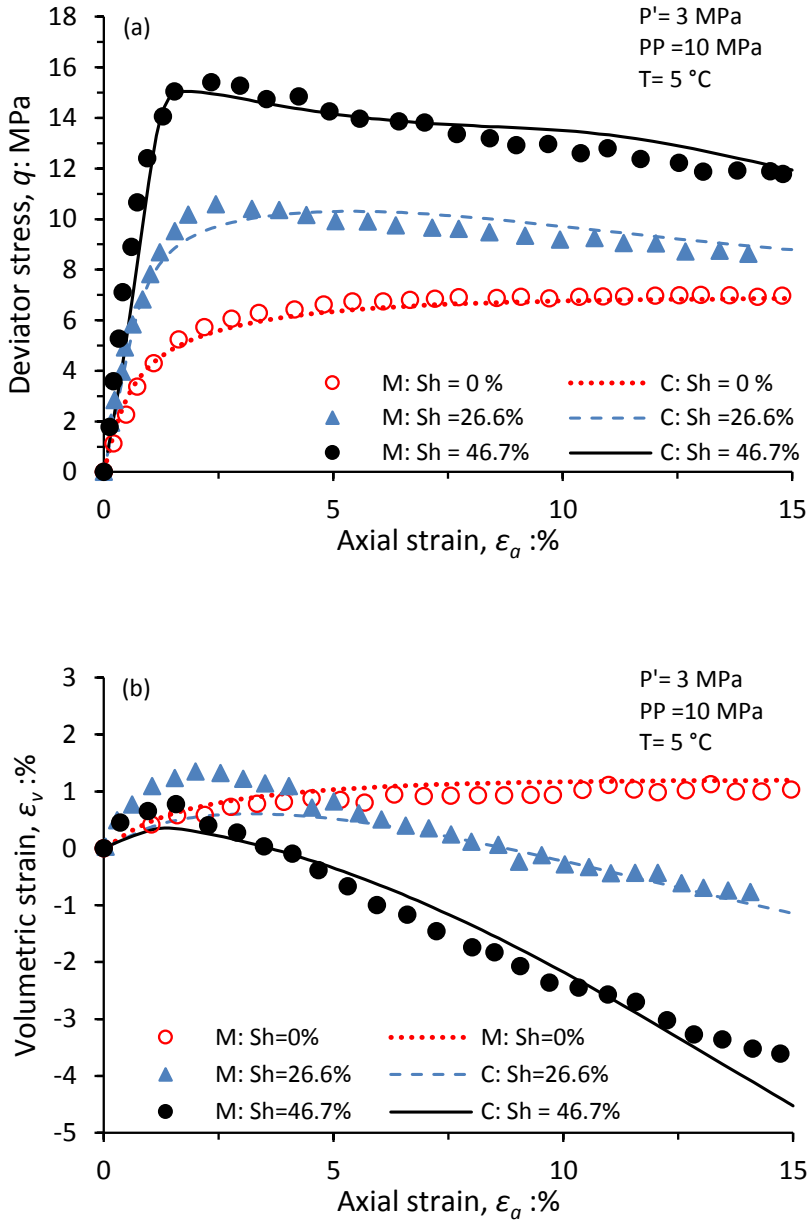

Fig. 7. Comparison of the measured and computed results of gas-saturated MHBS with different degrees of hydrate saturation: (a) stress-strain behaviour; (b) volumetric response

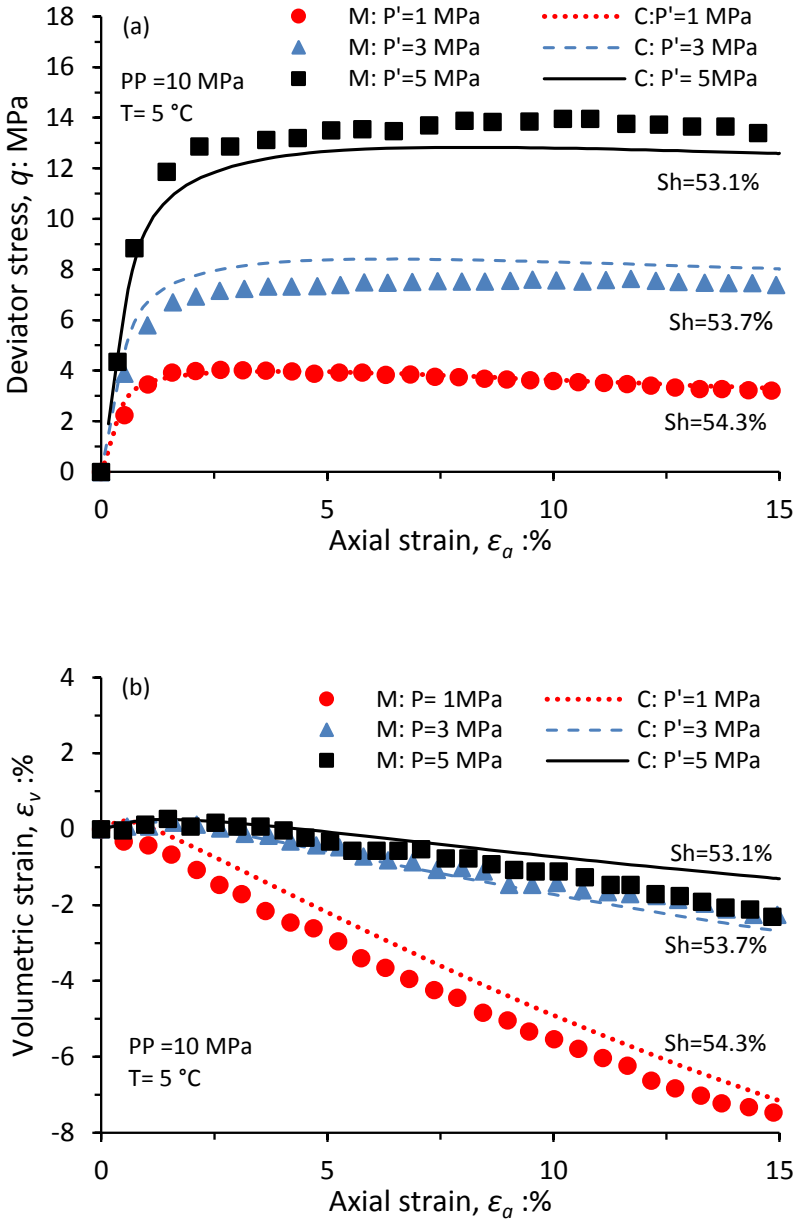

Fig. 8. Comparison of the measured and computed results of water-saturated MHBS at different effective confining pressures: (a) stress-strain behaviour; (b) volumetric response

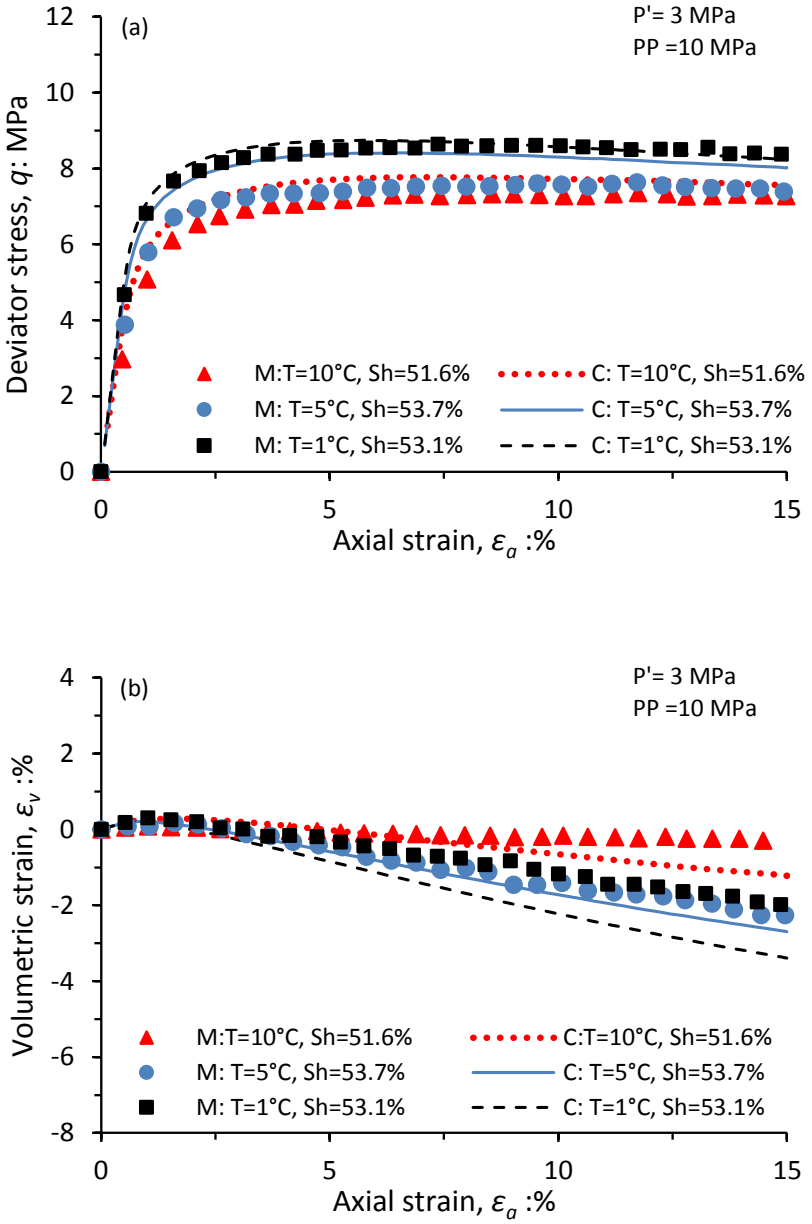

Fig. 9. Comparison of the measured and computed results of water-saturated MHBS at different temperatures: (a) stress-strain behaviour; (b) volumetric response

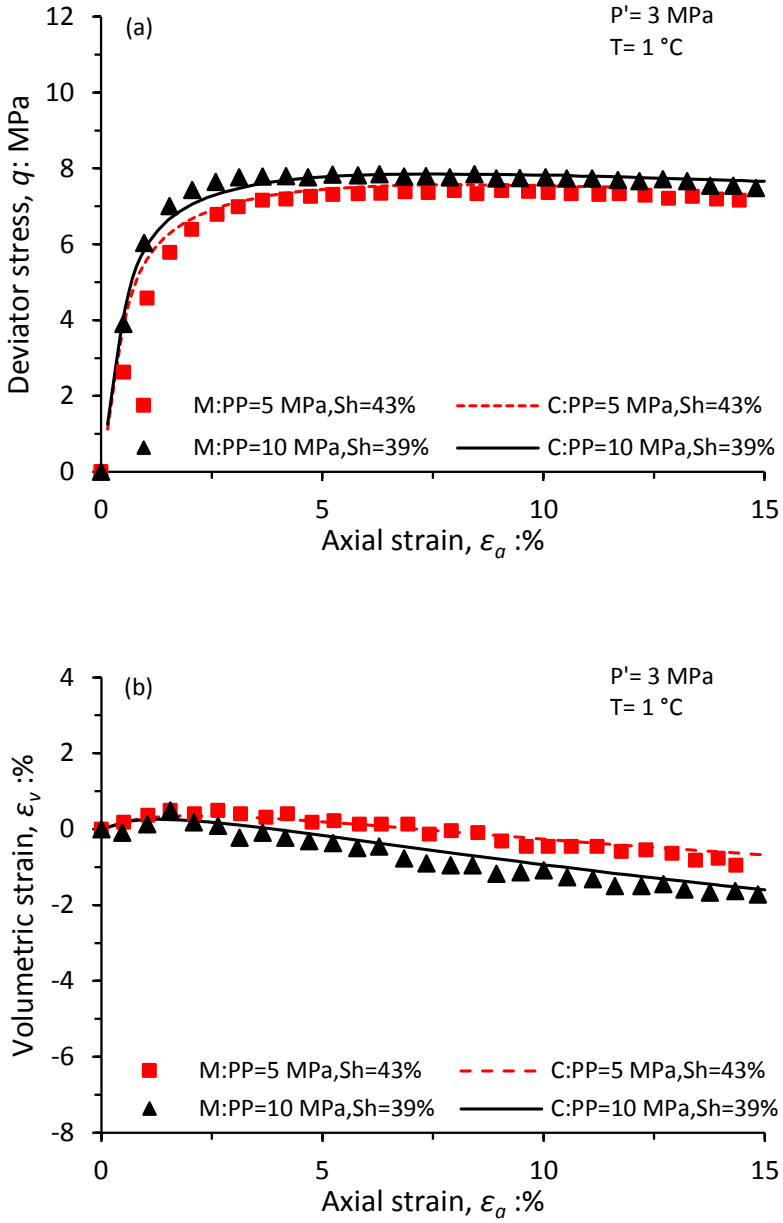

Fig. 10. Comparison of the measured and computed results of water-saturated MHBS at different pore pressures: (a) stress-strain behaviour; (b) volumetric response

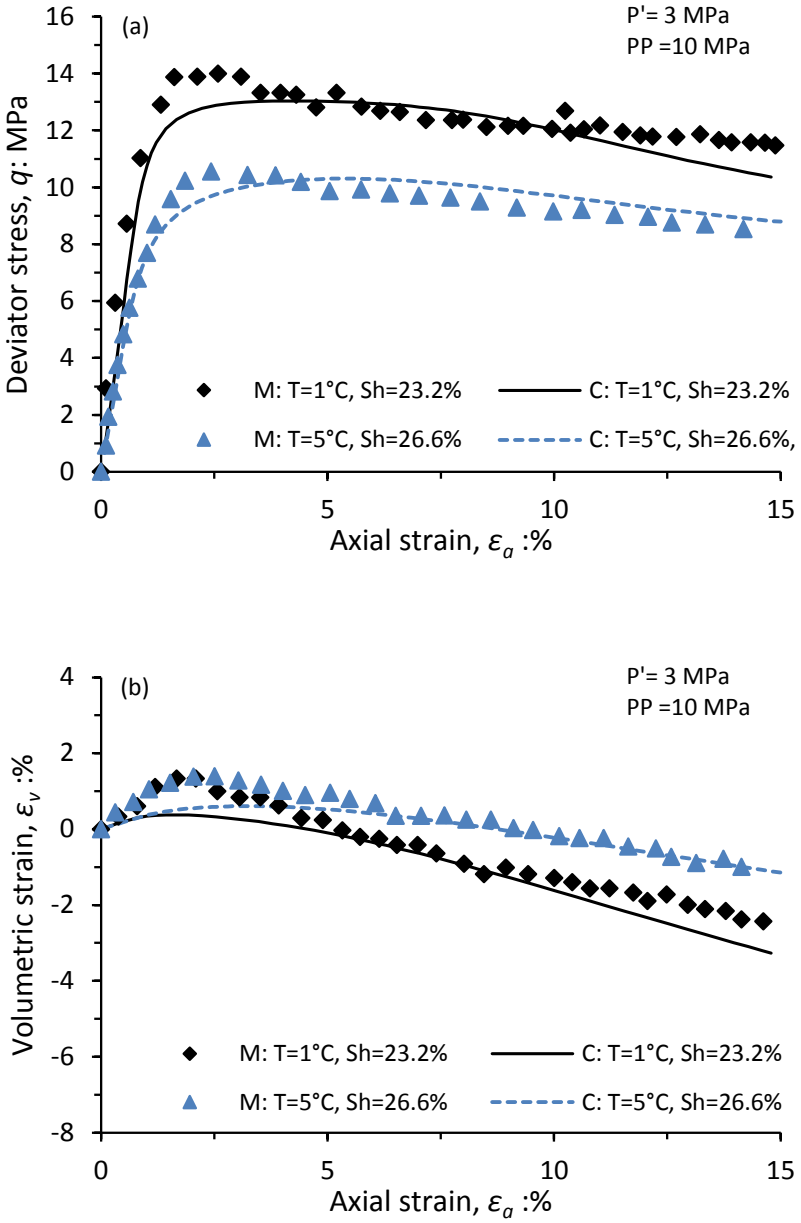

Fig. 11. Comparison of the measured and computed results of gas-saturated MHBS at different temperatures: (a) stress-strain behaviour; (b) volumetric response

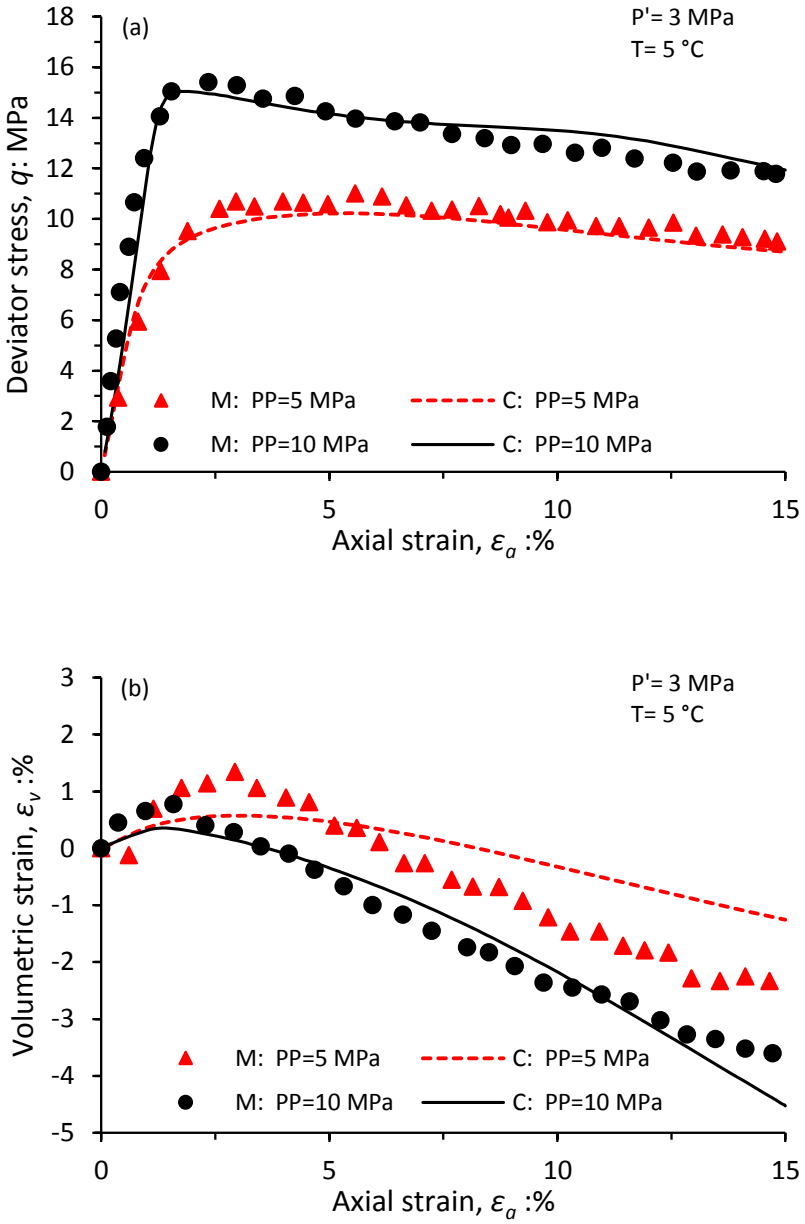

Fig. 12. Comparison of the measured and computed results of gas-saturated MHBS at different pore pressures: (a) stress-strain behaviour; (b) volumetric response